RSC Advances

PAPER

View Article Online
View Journal | View Issue

Cite this: *RSC Adv.*, 2018, **8**, 3858

Synthesis of CrO_x/C catalysts for low temperature NH_3-SCR with enhanced regeneration ability in the presence of SO_2†

Shuohan Yu,[ab] Sheng Xu,[c] Bowen Sun,[ab] Yiyang Lu,[ab] Lulu Li,[ab] Weixin Zou,[ab] Peng Wang,[c] Fei Gao,*[ab] Changjin Tang[ab] and Lin Dong*[ab]

Received 31st August 2017
Accepted 22nd December 2017

DOI: 10.1039/c7ra09680a

rsc.li/rsc-advances

Chromium oxide nano-particles with an average diameter of 3 nm covered by amorphous carbon (CrO_x/C) were successfully synthesized. The synthesized CrO_x/C materials were used for the selective catalytic reduction of NO_x by NH_3 (NH_3-SCR), which shows superb NH_3-SCR activity and in particular, satisfactory regeneration ability in the presence of SO_2 compared with Mn-based catalysts. The as-prepared catalysts were characterized by XRD, HRTEM, Raman, FTIR, BET, TPD, TPR, XPS and *in situ* FTIR techniques. The results indicated presence of certain amounts of unstable lattice oxygen exposed on the surface of CrO_x nano-particles with an average size of 3 nm in the CrO_x/C samples, which led to NO being conveniently oxidized to NO_2. The formed NO_2 participated in NH_3-SCR activity, reacting with catalysts *via* a "fast NH_3-SCR" pathway, which enhanced th NH_3-SCR performance of the CrO_x/C catalysts. Furthermore, the stable lattice of the CrO_x species made the catalyst immune to the sulfation process, which was inferred to be the cause of its superior regeneration ability in the presence of SO_2. This study provides a simple way to synthesize stable CrO_x nano-particles with active oxygen, and sheds light on designing NH_3-SCR catalysts with highly efficient low temperature activity, SO_2 tolerance, and regeneration ability.

1. Introduction

Low-temperature NH_3-SCR (<200 °C), which can be located downstream of electrostatic precipitators and even desulfurizers, where most of SO_2 and dust have been removed, has been paid increasing attention in the past few decades.[1–4] Various transition metal oxides exhibit satisfactory activity for low-temperature NH_3-SCR, such as Mn, Fe, Cu, and Co.[2,5–9] Among them, Mn-based catalysts have become a focus for their excellent low-temperature activity and inherent environment-friendly nature.[4,10–12] According to literature, Mn-based catalysts have a unique advantage for low-temperature SCR (<200 °C) in contrast with other competitors. For example, Hu *et al.* reported a Co–Mn/TiO_2 catalyst with superior NH_3-SCR activity at 200 °C.[11] Mn–Ce–Ti mix-oxide catalysts were recorded to exhibit an operating temperature window from 150 °C to 200 °C.[12] We also reported Mn–Fe–Ti mix-oxide catalysts with satisfactory NH_3-SCR activity from 100 °C to 350 °C.[5] However, the poor SO_2 resistance performance of Mn-based catalysts limits their practical application.

According to the previous reports,[4,13–15] the tolerance of metal oxide based catalysts to SO_2 depends on the type and oxidation state of the deposited metal, the nature of the support, and the type of reducing agent. In general, the rapid deactivation of NH_3-SCR catalysts involves two main mechanisms. One is the formation of ammonium salts.[14,16–22] The SO_2 in the feed gas can be oxidized to SO_3 on the surface of the catalysts, and the formed SO_3 would respond to NH_3 and water in feed gas transforming to NH_4HSO_4. The formed NH_4HSO_4 would deposit on the surface of the catalysts, cover active sites, block pores of the catalysts, and result in the deactivation of the catalysts. The other fact is the irreversible sulfation of the active phase.[14,16,18–23] For most transition metal oxides usually reported as NH_3-SCR catalysts, such as Mn, Fe, Cu, and Co, all sulfating processes are spontaneous according to their Gibbs free energy values (Table S1†). In the sulfation process, formation of a metal sulfate requires breaking the metal oxide lattice. It is reasonable to predict that the more stable the metal oxides, the more difficult it is to break the metal oxide lattice and thus, harder is the sulfation of metal oxide. In general, the metal oxide with a high melting point has

[a]Key Laboratory of Mesoscopic Chemistry of MOE, School of Chemistry and Chemical Engineering, Nanjing University, Nanjing 210093, PR China. E-mail: donglin@nju.edu.cn; gaofei@nju.edu.cn

[b]Jiangsu Key Laboratory of Vehicle Emissions Control, Center of Modern Analysis, Nanjing University, Nanjing 210093, PR China

[c]National Laboratory of Solid State Microstructures, College of Engineering and Applied Sciences, Collaborative Innovation Center of Advanced Microstructures, Nanjing University, Nanjing 210093, China

† Electronic supplementary information (ESI) available: Band energy calculation, thermochemical data, band energy data, mass of metal sulfate formed on catalysts, surface atomic concentration of SO_2 poisoned CrO_x/C-450 sample, extra NH_3-SCR and water tolerance tests, XRD patterns, FTIR data, Raman data, extra TEM image, NH_3-TPD data, H_2-TPR data, O_2-TPD data, extra XPS spectra. See DOI: 10.1039/c7ra09680a

a stable crystal lattice. Thus, the melting point can be an indicator of the stability of the crystal lattice of metal oxides.[24] In the case of Mn-based catalysts, MnO_2 has a low melting point (Table S1†), indicating its unstable structure, which is the cause of the severe irreversible sulfation of MnO_2 in the NH_3-SCR process, particularly in the low temperature range (<200 °C).[13,14,25–28] Cr_2O_3, which has the highest melting point among the transition metal oxides with NH_3-SCR activity (listed in Table S1†), was expected to have resistance to the sulfation process. Although the low NH_3-SCR activity of crystalline Cr_2O_3 is unsatisfactory, amorphous Cr_2O_3 exhibits superb low temperature NH_3-SCR activity, according to literature.[29–33] Thus, it appears to be a promising strategy to design a SCR catalyst with both low temperature activity and SO_2 tolerance *via* enhancing the catalytic activity of crystalline Cr_2O_3.

Compared with traditional metal oxide catalysts with a large particle size, nano-sized catalysts often have significant amounts of unsaturated-coordinated atoms exposed on their surfaces. Unsaturated-coordinated atoms are usually active; thus, nano-sized catalysts exhibit unique redox ability and enhanced catalytic activity.[34–36] Therefore, decreasing the size of catalysts appears to be a promising strategy to enhance low temperature NH_3-SCR performance of crystalline Cr_2O_3. However, nano-particle materials have the disadvantage of instability and tend to aggregate due to their high surface energy and their abundant surface unsaturated atoms. Recently, metal oxide nano-particles catalysts derived from MOFs material were reported.[37–39] Through a thermal decomposition process under controlled atmosphere, MOFs built from metal ions or nodes and polyfunctional organic ligands can transform into nano-materials, including nano-particles, single atoms, and metal oxide clusters. Wu *et al.*[40] synthesized Co nano-particles and single atoms from Co MOF and Co/Zn bimetallic MOF. Similar results were also reported by Li *et al.*[37] and Sun's group.[41] The carbon from the organic ligands of MOFs remains in materials and can protect metal oxide nano-particles from aggregation.

Herein, novel CrO_x nano-particles covered by amorphous carbon (CrO_x/C) have been synthesized by a MOFs assisted process for low temperature NH_3-SCR. MIL-101, with a metal node of 3 Cr atoms,[42,43] was employed as a precursor. The results of the catalytic tests for NH_3-SCR showed that the prepared CrO_x catalyst exhibited satisfactory activity and superior regeneration ability. According to a series of characterizations, the CrO_x/C catalyst was observed to be composed of CrO_x nano-particles with an eskolaite phase and activated lattice oxygen. It was deduced that the activated lattice oxygen was closely related to the enhanced NH_3-SCR activity of the CrO_x/C catalyst. The stable lattice of the eskolaite phase-CrO_x inhibited the sulfating process, thus causing the SO_2 tolerance and regeneration ability. To the best of our knowledge, it is the first time that a non-Mn catalyst with excellent low temperature NH_3-SCR activity and remarkable regeneration ability has been reported. This study provides a simple route to synthesize stable CrO_x nano-particles with active oxygen and shed light on designing low temperature NH_3-SCR catalysts with SO_2 tolerance and regeneration ability.

2. Experimental details

2.1. Preparation of catalysts

Typically, MIL-101(Cr) was prepared by reacting terephthalic acid (332 mg, 2.0 mmol) with $Cr(NO_3)_3 \cdot 9H_2O$ (800 mg, 2.0 mmol) and de-ionized water (9.5 mL) at 220 °C for 8 h. Microcrystalline green powders of MIL-101(Cr) were produced during the reaction. The obtained powders were washed by ammonium hydroxide, water, and ethanol, in sequence, 3 times each. The powders were dried and calcined at a certain temperature for 4 h under N_2 flow, and the heating rate was set at 1 °C min^{-1}. Finally, the cooled sample was exposed to air and denoted as Cr_2O_3/C-*X*, in which *X* represents the calcining temperature.

As reported in ref. 44, a Cr_2O_3 sample was obtained by calcining $Cr(NO_3)_3 \cdot 9H_2O$ at 450 °C for 4 h. MnO_2 was purchased from Aladdin and was used without further purification. An active carbon supported Cr_2O_3 catalyst was synthesized through a wetness impregnation process. Active carbon (1.00 g) was dispersed into de-ionized water (50 mL) containing $Cr(NO_3)_3 \cdot 9H_2O$ (9.92 g). The turbid solution was oil-bath heated at 110 °C until the water was totally evaporated. The dried powders were calcined at 450 °C for 4 h under a N_2 flow and the obtained sample was noted as Cr_2O_3/C-WI.

2.2. Characterizations

The X-ray diffraction (XRD) patterns of the catalysts were studied using an XRD-6000 X-ray diffractometer (Shimadzu). X-ray fluorescence (XRF) analysis was performed on an ARL-900 X-ray fluorescence analyzer. FTIR analysis was carried out using a NEXUS870 spectrometer (NICOLET, America). Raman spectra were measured at a resolution of <1 cm^{-1} using a JY Labram HR 800 spectrophotometer equipped with an argon-ion laser source and an air-cooled CCD detector. N_2 adsorption/desorption isotherms of the catalysts were obtained at −196 °C using an ASAP2020 physical adsorption instrument (Micromeritics) to calculate the BET surface area of the catalysts. TEM analysis was performed on a double-aberration corrected Titan™ cubed G2 60-300 S/TEM equipped with Super-X™ technology. X-ray energy dispersive spectroscopy (EDS) mappings were acquired using the Super-X EDS system, which is composed of four silicon drift detectors covering 0.7 s rad collection.

NH_3-temperature programmed desorption (NH_3-TPD) experiments were performed using a multifunction chemisorption analyzer, equipped with a thermal conductivity detector (TCD). Samples were pretreated under a NH_3–N_2 flow (NH_3 1%) at 150 °C for 1 h and were heated under N_2 flow; the heating rate was set at 10 °C min^{-1}.

O_2-temperature programmed desorption (O_2-TPD) experiments were performed using a multifunction chemisorption analyzer, equipped with a thermal conductivity detector (TCD). Samples were pretreated under O_2–He flow (O_2 25%) at 25 °C for 1 h and were heated under a He flow; the heating rate was set at 10 °C min^{-1}.

H_2-temperature programmed reduction (H_2-TPR) of the catalysts was recorded using a chemisorption analyzer. Samples were pretreated under a N_2 flow at 200 °C for 1 h, and were heated under a H_2–Ar flow (H_2, 7%); the heating rate was set at 10 °C min^{-1}.

X-ray photoelectron spectroscopy (XPS) measurements were performed using a PHI 5000 VersaProbe spectrophotometer. The contents of the metal ions were measured *via* an inductive coupled plasma emission spectrometer (Optima 5300DV, PE). Energy referencing was accomplished by setting the adventitious carbon peak to 284.6 eV. The *ex situ* XPS details are described below. The sample was treated under a certain atmosphere for a certain time in a reaction chamber connected with the intro chamber of the XPS instrument. Following this, the reaction chamber was vacuumized and the treated sample was transferred to the XPS instrument without exposure to air.

The *in situ* DRIFT experiments were performed on a Nicolet Nexus 5700 FTIR spectrometer using a diffuse reflectance attachment (HARRICK) equipped with a reaction cell (ZnSe windows). The number of scans was 32 at a resolution of 4 cm^{-1} and the spectra were presented as Kubelka–Munk function, referred to the background spectra of the recorded catalyst in N_2.

2.3. NO oxidation tests

The NO oxidation tests were performed in a fixed-bed reactor with 0.2 g catalyst. The feed gas contained 500 ppm NO and 5 vol% O_2 with N_2 as the balance gas. The total flow rate of the feed gas was 100 mL min^{-1}, corresponding to a space velocity of approximately 30 000 h^{-1}. Including NO and NO_2, the effluent gases were continuously analyzed at 150 °C by an online Thermofisher IS10 FTIR spectrometer equipped with a 2 m path-length gas cell (250 mL volume).

2.4. NH_3-SCR activity, SO_2 poisoning, and regeneration tests

The NH_3-SCR activity tests were performed in a fixed-bed reactor with 0.2 g catalyst. The feed gas contained 500 ppm NO, 500 ppm NH_3, 5 vol% O_2, 50 ppm SO_2 (when used), 5 vol% H_2O (when used) and N_2 as the balance gas. The total flow rate of the feed gas was 100 mL min^{-1}, corresponding to a space velocity of approximately 30 000 h^{-1}. SO_2 poisoning and regeneration tests of catalysts were carried out at 150 °C. Including NO, NH_3, NO_2, and N_2O, the effluent gases were continuously analyzed at 150 °C using an online Thermofisher IS10 FTIR spectrometer equipped with a 2 m path-length gas cell (250 mL volume).

2.5. Regeneration of SO_2 poisoned catalysts

SO_2 poisoned catalysts were regenerated at 300 °C for 30 min, and then were cooled down to room temperature. All the heat treatments were carried out under N_2 atmosphere.

The sulfating of metal oxide catalysts during SO_2 poisoning was investigated by inductively coupled plasma-emission spectroscopy (ICP).

The SO_2-poisoned catalyst (0.2 g) was washed with deionized water for 5 times. The eluate was collected and diluted to 50 mL. The diluted eluate was investigated by ICP analysis. The contents of metal sulfate m_{MSO_4} were calculated using the equation below.

$$m_{MSO_4} = \frac{m_{M^{n+}} \times 0.05L \times M_{MSO_4}}{M_M}$$

where, $m_{M^{n+}}$ is the content of the metal ion, M_{MSO_4} was obtained *via* ICP analysis and M_M is the molar mass of metal sulfate, which also corresponds to the molar mass of the metal ion.

For Cr oxide, $m_{Cr_2(SO_4)_3} = m_{Cr^{3+}} \times 0.188$

For Mn oxide, $m_{MnSO_4} = m_{Mn^{2+}} \times 0.137$

3. Results and discussion

3.1. NH_3-SCR performance, SO_2 tolerance, and regeneration

The NH_3-SCR activities of the CrO_x samples derived from various precursors and MnO_2 are shown in Fig. 1 and S1†. As it was anticipated, all the catalysts derived from MIL-101 exhibited superior activities than pure Cr_2O_3. Remarkably, CrO_x/C-450, parallel to MnO_2, exhibited a wide operation temperature window from 125 °C to 200 °C. The activity of Cr_2O_3/C-WI was enhanced compared with pure Cr_2O_3, while it was much lower than CrO_x/C-450. This extraordinarily low temperature NH_3-SCR performance makes CrO_x/C-450 the best catalyst among all the samples derived from MIL-101. To evaluate the NH_3-SCR performances on the catalysts more precisely, the normalized rates per mole transition metal were calculated and the results are displayed in Fig. 2a. The catalytic activity order is CrO_x/C-450 > Mn_2O_3 > Cr_2O_3/C-WI > Cr_2O_3. In addition, the apparent active energies of CrO_x/C-450 and Cr_2O_3 based catalysts were obtained when NO conversions were limited to low conversion (Fig. 2b and Table S2†). The apparent active energy of NH_3-SCR on the CrO_x/C-450 catalyst was lower than those of SCR on Cr_2O_3/C-WI and Cr_2O_3, which further confirms the superb catalytic activity of the CrO_x/C-450 sample. Based on the kinetics data listed in Tables S3 and S4,† apparent kinetics equations of NH_3-SCR on CrO_x/C-450 and Cr_2O_3/C-WI catalysts were obtained (Fig. S2†). For CrO_x/C-450, $r = [NH_3]^{0.586}[NO]^{0.964}$ at 150 °C, while for Cr_2O_3/C-WI, $r = [NH_3]^{0.433}[NO]^{0.092}$. The different reaction rate equations of NH_3-SCR on CrO_x/C-450 and Cr_2O_3/C-WI catalysts indicated their different reaction mechanisms, which may result in different NH_3-SCR performance of CrO_x/C-450 and Cr_2O_3/C-WI catalysts. The N_2 selectivity of CrO_x/C-450 remained at a high level (over 90%) in its operation temperature window, while those of Cr_2O_3 and MnO_2 were very poor. This indicated that side reactions such as the formation of N_2O hardly occurred on the CrO_x/C-450 catalyst. SO_2- and H_2O-tolerance of CrO_x/C-450 was further tested and the results are presented in Fig. 1c and S1c.† CrO_x/C-450 exhibited over 80% NO conversion within 24 h in the presence of H_2O, indicating its satisfactory water tolerance. When SO_2 was introduced into the feed gas, the activity of CrO_x/C-450 gradually dropped to 60% within 20 h, while it dropped to 50% in 20 h when SO_2 and H_2O co-existed in the feed gas. The activity of CrO_x/C-450 could be recovered after a heat treatment at a temperature as low as 300 °C. This indicated that the poisoning effect of SO_2 on CrO_x/C-450 could be accelerated by H_2O, while H_2O hardly influenced the regeneration ability of CrO_x/C-450. In contrast, the MnO_2 catalyst

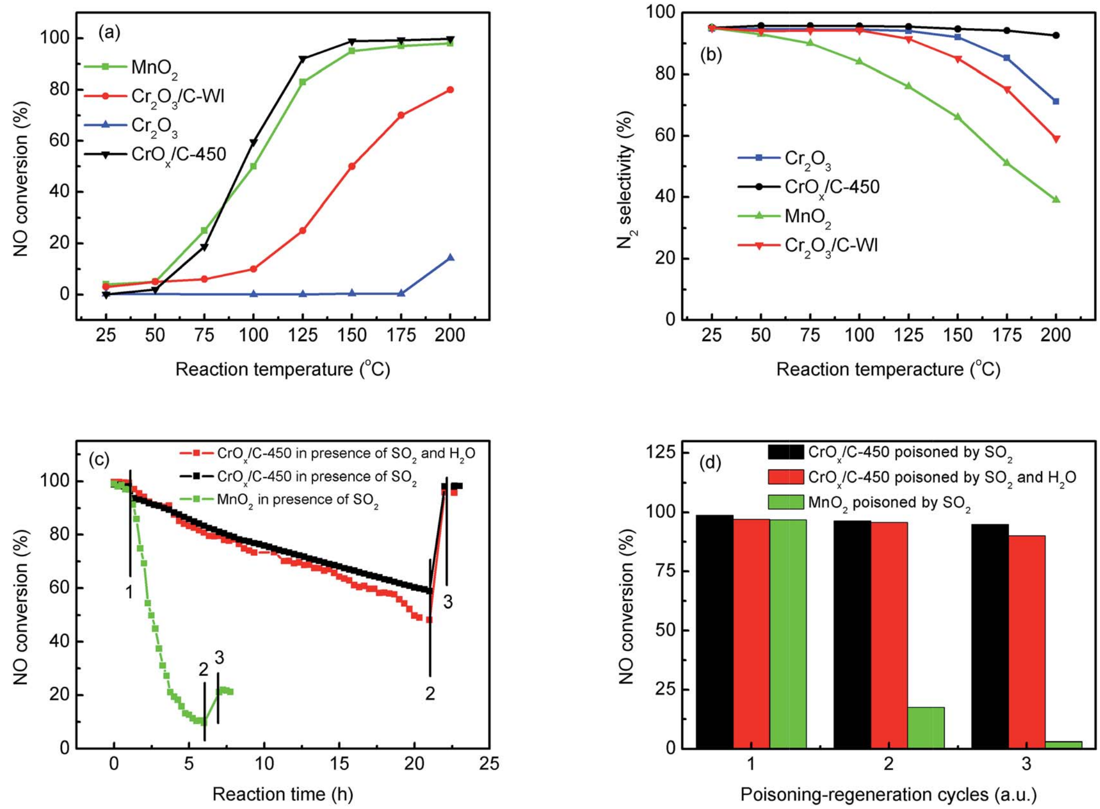

Fig. 1 NH_3-SCR activity of catalysts: (a) NO conversion, (b) N_2 selectivity, (c) SO_2 poisoning test (step 1, 2, and 3 present SO_2 and H_2O (when used) on, SO_2 and H_2O (when used) off, and after regeneration), and (d) regeneration ability.

deactivated rapidly upon SO_2 introduction in 6 h, and this process was irreversible. It was demonstrated that the CrO_x/C-450 catalyst has satisfactory SO_2-tolerance. The regeneration ability of CrO_x/C-450 was further studied. As shown in Fig. 1d, over 90% of the catalytic activity of CrO_x/C-450 could be recovered as compared to that of the fresh catalyst after 3 poisoning–regeneration cycles irrespective of whether H_2O was introduced by regeneration at 300 °C in flowing N_2, while that of MnO_2 catalyst dropped dramatically through only 1 poisoning–regeneration cycle, which indicated the remarkable regeneration ability of the CrO_x/C-450 sample.

3.2. Structural information

To investigate the NH_3-SCR on the catalysts, the structural information of catalysts was necessary. XRD, XRF, FTIR, Raman, and TEM analyses were carried out to investigate the structural properties of the catalysts synthesized from MIL-101(Cr). The XRD patterns of all samples are shown in Fig. S3.† In the XRD pattern of the precursor, sharp and distinct peaks attributed to the MIL-101 phase were detected, which is in agreement with the data reported by Jhung *et al.*[43] When MIL-101 was heated in N_2-flow, the XRD peaks of MIL-101 became weak and gradually disappeared with an increase in

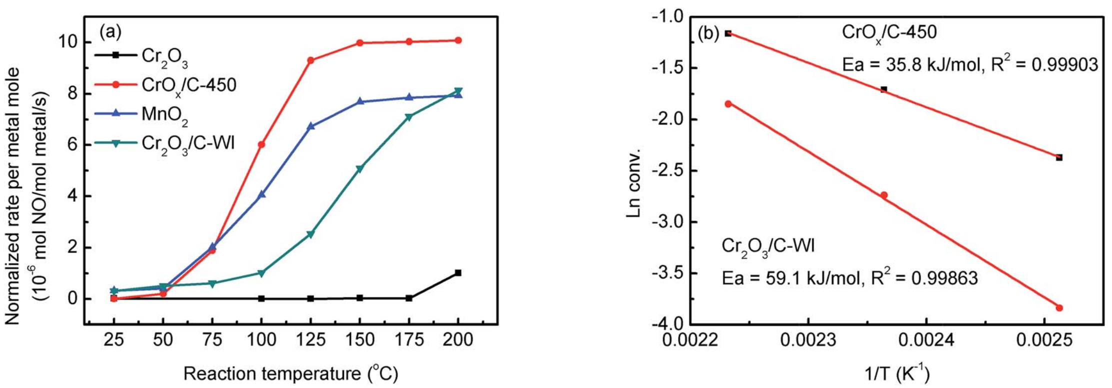

Fig. 2 (a) Normalized rates per metal mole of catalysts, (b) apparent active energy of CrO_x/C-450 and Cr_2O_3/C-WI catalysts.

temperature. When the calcining temperature reached 450 °C, the peaks of the MIL-101 phase disappeared completely and replaced with wide and weak peaks at 24.5°, 33.5°, and 36.1°, which belonged to the (012), (104), and (110) plane, respectively, of the eskolaite phase (PDF#38-1479) as well as Cr_2O_3/C-WI.[45] This indicated that the MIL-101 structure could be destroyed through the calcining process, accompanied with the formation of the eskolaite phase. Furthermore, the CrO_x/C-450 sample was found to have a small particle size based on its broad XRD peaks.

FTIR and Raman analyses were carried out to study the carbon species in the catalysts. As shown in Fig. S4a,† the bands at 3300 cm^{-1}, 1600 cm^{-1}, and 1400 cm^{-1} were identified in the FTIR spectra of MIL-101. The broad band at 3300 cm^{-1} arises due to the stretching vibration of the surface –OH groups. The two bands at 1600 and 1400 cm^{-1} could be attributed to the stretching vibration of the –COO group of the organic linkers of MIL-101. However, the intensity of bands at 1600 cm^{-1} and 1400 cm^{-1} decreased on increasing the calcination temperature. This indicates that the organic linker begins to decompose and carbonize when the calcining temperature increases. The carbonization process was further investigated by Raman analysis (Fig. S4b†). Wide bands at 1360 and 1590 cm^{-1}, corresponding to the D-band and G-band of MIL-101, were detected in the samples calcined at low temperatures, such as 350 and 400 °C. When the calcining temperature increased, the G-band gradually disappeared and the D-band still remained, which indicated the loss of the ordered structure of MOFs and the formation of amorphous carbon. In the spectrum of Cr-550, the G-band disappeared absolutely and only a wide D-band was observed. This illustrates that the organic linker carbonized and transformed to amorphous carbon during the calcining process, which accompanied with the destruction of the MOFs structure.

The elemental contents of catalysts were studied *via* XRF analysis. Since the organic species in MIL-101 completely transformed to amorphous carbon in CrO_x/C-450, as mentioned before, the ignition loss in XRF analysis of CrO_x/C-450 was believed to be the result of carbon species burning. Thus, the elemental contents of the catalysts could be calculated from the XPF data and the results are shown in Table 1. The CrO_x/C-450 catalyst consisted of 19.2% Cr, 28.7% O, and 52.0% C. As it was designed, the elemental contents of Cr_2O_3/C-WI were similar to those of CrO_x/C-450.

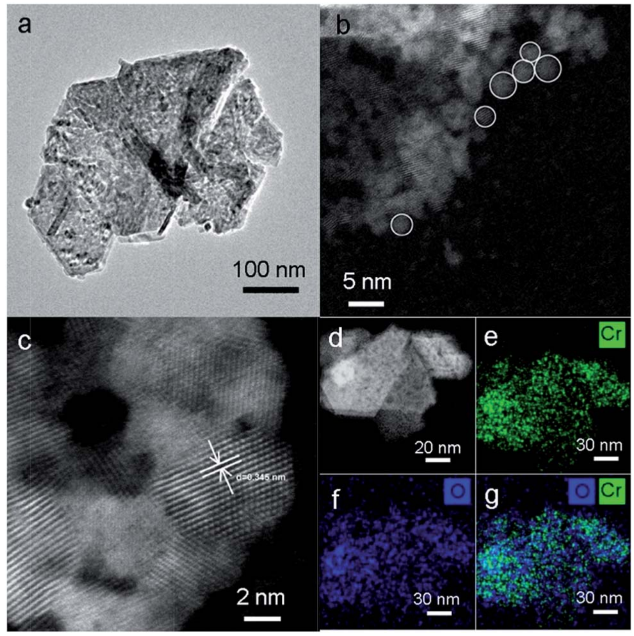

Fig. 3 (a) TEM image, (b–d) high resolution HAADF-STEM image of CrO_x/C-450 catalyst. (e, f) 2D STEM EDS elemental maps of Cr-Kα (Green) and O (Blue) elements, respectively. (g) A superimposed image of (e) and (f).

TEM analysis was performed to investigate the structure of MIL-101, CrO_x/C-450, and Cr_2O_3/C-WI. As shown in Fig. S5a,† the MIL-101 with octahedron morphology can be observed distinctly, while it transformed to a hexagonal sheet after calcination (Fig. 3a). Further structural information was obtained *via* high-angle annual dark field (HAADF) imaging (Fig. 3b). The hexagonal-like sample observed in Fig. 3a was actually an aggregation of nano-particles with an average size of 3 nm. In addition, lattice fringes of $d = 0.345$ nm were observed (Fig. 3c), corresponding to the eskolaite Cr_2O_3 (012) crystal plane, which further confirmed that the Cr oxide in the CrO_x/C-450 catalyst has the eskolaite phase. From the EDX element mapping analysis (Fig. 3e–g), Cr element and O element were observed to be highly dispersed in the CrO_x/C-450 sample and the superimposed image of Cr and O matches the HAADF image. It was estimated that the CrO_x/C-450 catalyst was primarily formed by CrO_x nano-particles with eskolaite phase as

Table 1 Element contents and surface areas of catalysts

	Contents[a] (wt%)		Elements contents (at%)			Surface area[b] (m^2 g^{-1} catalyst)		
Sample	Cr_2O_3	Ignition loss	Cr	O	C	Sample	Carbon support[c]	Active material
CrO_x/C-450	70.2	29.8	19.2	28.7	52.0	256	784	20.8
Cr_2O_3/C-WI	69.5	30.5	18.9	28.4	52.7	279	897	9.9
Cr_2O_3	99.9	0.1	40.0	60.0	—	28	—	—

[a] Contents of catalysts were obtained from XRF analyses. [b] Surface areas of catalysts were obtained from N_2 adsorption/desorption analyses. [c] Carbon support of CrO_x/C-450 catalyst was obtained by washing CrO_x/C-450 using hydrochloric acid. Carbon support of Cr_2O_3/C-WI is active carbon.

designed in this study. The CrO_x/C-450 sample after 3 poisoning–regeneration cycles was also imaged to investigate the stability of the catalyst (Fig. S5b†). The used sample was primarily composed of CrO_x nano-particles, similar to the fresh sample, and no major difference in the particle size of Cr_2O_3 could be observed after 5 deactivation–regeneration circles, which evidently proved the stability of the sample CrO_x/C-450. Cr_2O_3 and Cr_2O_3/C-WI, however, had a bulk-like shape (Fig. S5c and d†) with average particle sizes of over 100 nm. In the structure of the MIL-101 precursor, metal nodes containing 3 Cr atoms were covered by organic linkers. Therefore, it is reasonable to suggest that CrO_x nano-particles in the CrO_x/C-450 catalyst stabilized by covering carbon species transformed from organic linkers of MIL-101 after the calcining process.

The feasible mechanism of catalyst synthesis is displayed in Fig. 4. During the calcination process, organic linkers covering Cr nodes carbonized and the structure of MIL-101 gradually destroyed. The amorphous carbon from organic linkers limited the growth of Cr nodes. Finally, when the calcined sample was exposed to air, the remaining Cr nano-particles were oxidized to CrO_x nano-particles with eskolaite phase, forming the structure of amorphous carbon covered CrO_x nano-particles (CrO_x/C).

3.3. Textural properties of catalysts

As mentioned before, the CrO_x/C-450 catalyst was primarily formed by CrO_x nano-particles with eskolaite phase and exhibited enhanced NH_3-SCR activity and satisfying regeneration ability. To explore the relationship between the structure of CrO_x/C-450 and the NH_3-SCR performance, the properties of the catalysts were characterized by BET, XPS, H_2-TPR, O_2-TPD, and NH_3-TPD analyses.

The surface areas of the catalysts can influence the number of active sites on the catalyst surface, which is considered as an important fact affecting the catalytic activity of NH_3-SCR catalysts. The surface areas of CrO_x/C-450, Cr_2O_3, and Cr_2O_3/C-WI obtained from BET analysis are listed in Table 1. The BET surface areas of CrO_x/C-450 and Cr_2O_3/C-WI are similar and larger than that of Cr_2O_3. Due to the enhanced NH_3-SCR performances of CrO_x/C-450 and Cr_2O_3/C-WI (Fig. 1), it is believed that the enlarged surface area increased the activity of the Cr oxide catalyst. According to the reaction rates normalized by the surface areas of the active material of the catalysts, CrO_x/C-450 exhibited comparatively superior NO conversion than Cr_2O_3/C-WI at 125 °C and 150 °C. This infers that a large surface area is not the only reason for the excellent NH_3-SCR activity of CrO_x/C-450.

The acidity of the catalysts, which can influence the absorption of reaction agents, is an important factor affecting the NH_3-SCR performance of catalysts. This property of catalysts was investigated by NH_3-TPD analysis. As displayed in Fig. S6a,† the NH_3 desorption behaviours of Cr_2O_3 and CrO_x/C-450 were similar. No distinct NH_3 desorption peak was observed from 150 to 400 °C in the profiles of both Cr_2O_3 and CrO_x/C-450 samples, which indicated the weak acidity of these two samples. Therefore, the giant NH_3-SCR performance difference between Cr_2O_3 and CrO_x/C is not the result of acidity.

The redox ability of materials is another significant factor influencing the catalytic activity of the NH_3-SCR catalyst. H_2-TPR method was utilized to discuss this property of the synthesized catalysts. As illustrated in Fig. 5b, Cr_2O_3 exhibited a single-peak profile. The H_2 consumption peak at 343 °C was a result of one-step reduction from Cr^{6+} to Cr^{3+}, accompanied by the loss of lattice oxygen atoms connected with Cr^{6+} ions.[46] For

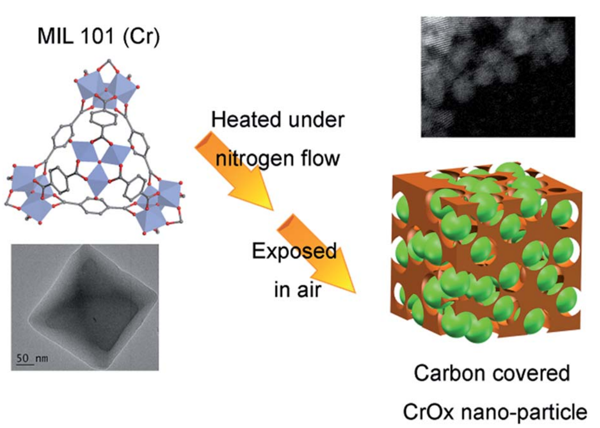

Fig. 4 Possible mechanism of catalyst synthesis (green spheres present CrO_x nano-particles, brown skolen present amorphous carbon).

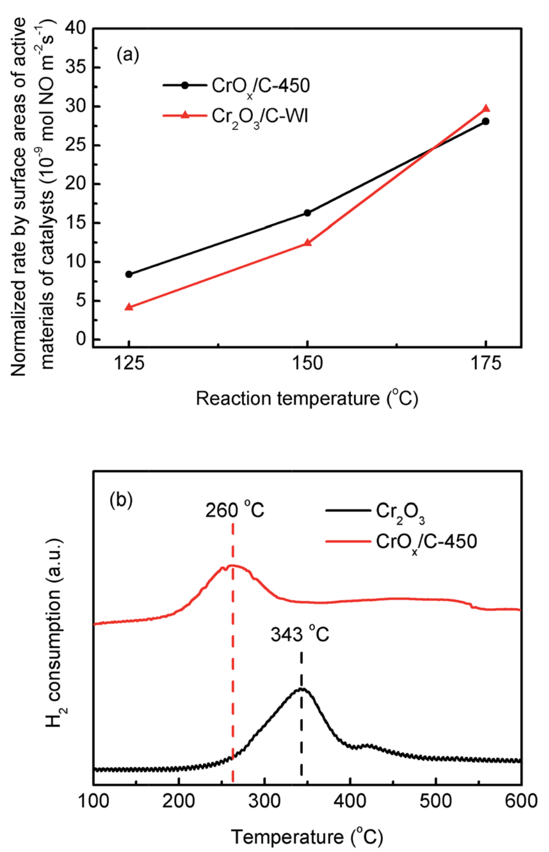

Fig. 5 (a) Normalized rates per surface areas of active material of CrO_x/C-450 and Cr_2O_3/C-WI catalysts, (b) H_2-TPR result of CrO_x/C-450 and bulk Cr_2O_3.

the CrO_x/C-450 sample, the H_2 consumption peak shifted to a low temperature, which indicated that CrO_x/C-450 exhibited stronger oxidation ability and a higher amount of active lattice oxygen than Cr_2O_3. In addition, O_2-TPD analysis was carried out to investigate the stability of the oxygen atoms of the catalyst; the results are shown in Fig. S6b.† In the profile of Cr_2O_3, no O_2 desorption peak was discovered in the temperature range from 50 °C to 450 °C, which indicates that the oxygen on the surface of Cr_2O_3 is stable and inert. However, the curve of CrO_x/C-450 exhibited an O_2 desorption peak from 200 to 350 °C, which was much higher than the desorption temperature of absorbed O_2 species recorded earlier.[47] Hence, the desorption peak from 200 to 350 °C was believed to correspond to the dissociation of lattice oxygen from CrO_x/C-450. This demonstrates that the lattice oxygen of CrO_x/C becomes more active and unstable than that of Cr_2O_3. Remarkably, the CrO_x/C catalyst has high surface atom/lattice atom rate for its ultrasmall size as mentioned before. It is reasonable to conclude that the unsaturated surface atoms of CrO_x/C cause the unique redox ability exhibited in H_2-TPR analysis and the instability of the lattice oxygen atom detected in O_2-TPD analysis. Unstable and activated oxygen atoms are inferred to enhance the activity of CrO_x/C catalyst.

In XPS analysis, Cr 2p spectra (Fig. 6a) of all the samples were comparable. The Cr $2p_{3/2}$ peak could be divided into two peaks at 576.7 eV and 578.6 eV, belonging to Cr^{3+} and Cr^{6+}, respectively.[48] The relative contents of Cr^{3+} and Cr^{6+} ions were analogous (Table 2), indicating their similar Cr state. The O 1s peak (Fig. 6b) could be separated into two peaks at 530.1 eV and 531.9 eV, attributed to the lattice oxygen and surface –OH groups, respectively.[49,50] The relative contents of these two types of oxygen species are also listed in Table 2. The CrO_x/C-450 sample exhibited more surface –OH groups than Cr_2O_3. Notably, the peak belonging to the lattice oxygen of CrO_x/C-450 shifts to the high binding energy side, contrasting with that of Cr_2O_3 and Cr_2O_3/C-WI. It is evident that the lattice oxygen of CrO_x/C-450 carries less negative charge than Cr_2O_3 and Cr_2O_3/C-WI. Materials with an ultrasmall size are deemed to have abundant dangling bands and their surface atoms are usually unsaturated-coordinated. In case of CrO_x/C-450, some surface oxygen atoms are inferred to be unsaturated coordinated for ultrasmall size of CrO_x nano-particles. This unsaturated oxygen is considered to have less negative charge and is expected to be more active than the saturated coordinated oxygen of bulk Cr_2O_3.

Furthermore, to determine whether the lattice oxygen participates in the NH_3-SCR reaction, *ex situ* XPS analysis was carried out. The CrO_x/C-450 catalyst was heated under NH_3 + NO flow at 150 °C for 1 h; the XPS spectra of CrO_x/C-450 before and after treatment are displayed in Fig. 6c and d. In the Cr 2p spectra (Fig. 6c), the peak of Cr^{6+} at 578.6 eV disappeared after NH_3 + NO treatment, while the peak of Cr^{3+} at 576.7 eV enhanced. This infers that Cr^{6+} species on the surface of CrO_x/C

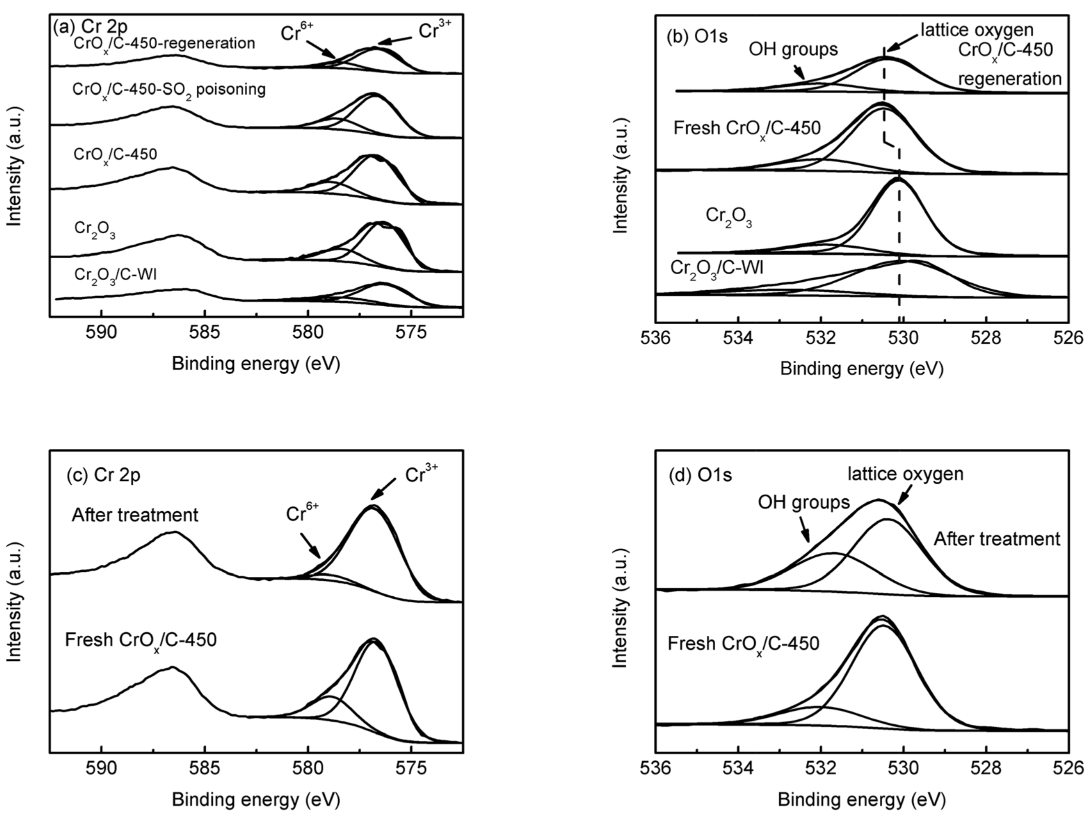

Fig. 6 XPS spectra of Cr_2O_3, fresh CrO_x/C-450 catalyst, SO_2 poisoned CrO_x/C-450 catalyst, and regenerated CrO_x/C-450 catalyst: (a) Cr 2p spectra, (b) O 1s spectra, and *ex situ* XPS analysis of fresh CrO_x/C-450 catalyst and CrO_x/C-450 catalyst heated under NH_3 + NO flow at 150 °C for 1 h: (c) Cr 2p spectra, (d) O 1s.

Table 2 Relative contents of Cr and O species on surfaces of catalysts

	Cr 2p		O 1s	
Sample	Cr^{3+a} (%)	Cr^{6+a} (%)	OH groups[a] (%)	Lattice oxygen[a] (%)
Cr_2O_3	76.74	23.26	13.39	86.61
CrO_x/C-450	78.86	21.14	18.36	81.64
CrO_x/C-450-regeneration	79.37	20.63	18.7	81.3
CrO_x/C-450 *ex situ* treatment	94.87	5.13	36.76	63.24
CrO_x/C-450-SO_2 poisoning	77.06	22.94	—	—

[a] Relative contents of Cr and O species were calculated from peak areas ratio of divided peaks in XPS spectra.

can react with the reagent molecules and eventually get consumed. Moreover, in the O 1s spectra (Fig. 6d), the peak intensity of lattice oxygen at 530.4 eV decreased after treatment, while the intensity of the peak attributed to the surface –OH group at 531.7 eV increased, which indicates the loss of surface lattice oxygen. Therefore, lattice oxygen was believed to take part in the NH_3-SCR on the CrO_x/C catalyst. Thus, CrO_x/C-450, which has more active lattice oxygen, can exhibit enhanced NH_3-SCR activity than Cr_2O_3.

3.4. Mechanism of NH_3-SCR on CrO_x/C catalyst

In "fast NH_3-SCR", NO catalytically reduced NH_3 in assistance of NO_2, which was reported to have lower activation energy and enhanced catalytic activity compared with the typical NH_3-SCR. Herein, the CrO_x/C catalyst was proved to have activated lattice oxygen. It is reasonable to deduce that NO can be oxidized to NO_2 by the activated oxygen on the CrO_x/C surface, making the NH_3-SCR on CrO_x/C proceed as the "fast NH_3-SCR" pathway. To verify this conjecture, NO oxidation on CrO_x/C-450 and Cr_2O_3/C-WI catalysts was carried out. As displayed in Fig. 7a, NO could be oxidized to NO_2 on both CrO_x/C-450 and Cr_2O_3/C-WI. However, the mass of formed NO_2 on CrO_x/C-450 exceeded as compared to that on Cr_2O_3/C-WI. Moreover, the normalized rate by surface area of NO oxidation on CrO_x/C-450 clearly surpassed that on Cr_2O_3/C-WI (Fig. 7b). This indicated that NO is more easily oxidized to NO_2 on CrO_x/C-450 catalyst with activated oxygen, which probably resulted in the superb NH_3-SCR performance of CrO_x/C-450.

In order to confirm whether the formed NO_2 participated in NH_3-SCR on the CrO_x/C catalyst, further information about the reaction mechanism was obtained using DRIFTS. In the spectra of the absorption NO + O_2 saturated CrO_x/C-450 sample (Fig. 8a), the bands centered at 1280, 1335, and 1520 cm^{-1}, and a wide band divided into bands at 1730, 1690, and 1660 cm^{-1} were detected. As reported elsewhere,[51] these IR bands were attributed to weakly bound NO_2 (1730 cm^{-1}), nitrite anion (1335 cm^{-1}), ν_s(N=O) and ν_{as}(N=O) of symmetric N_2O_3 (1690 and 1660 cm^{-1}), bidentate nitrates (1520 cm^{-1}), and monodentate nitrates (1280 cm^{-1}). When the feed gas was switched to NH_3, the bands belonging to NO_2 and bidentate nitrates gradually disappeared, replacing with the bands of NH_3 absorbed on Lewis acid sites (1620 and 1217 cm^{-1}),[52,53] while the bands corresponding to symmetric N_2O_3, nitrite anion, and monodentate nitrates were still present. Indeed, it is apparent that NO_2 and bidentate nitrates participated in the surface reaction on CrO_x/C-450 and were consumed by NH_3, which is a typical "fast NH_3-SCR" pathway.[54] To determine the role of NH_3, co-absorption of NO + O_2 on CrO_x/C-450 after pre-absorption of NH_3 was investigated (Fig. 8b). In the spectra of the absorption NH_3 saturated CrO_x/C-450 sample, only a weak band at 1620 cm^{-1} corresponding to NH_3 on Lewis acid sites was detected, indicating the low acidity of CrO_x/C-450 as mentioned in NH_3-TPD analysis. With the addition of NO and O_2, this band gradually disappeared, accompanied by the appearance of bands belonging to weakly bound NO_2 (1732 cm^{-1}), nitrite anion (1333 cm^{-1}), ν_s(N=O) and ν_{as}(N=O) of symmetric N_2O_3 (1691 and 1657 cm^{-1}), and bidentate nitrates (1515 cm^{-1}).[51]

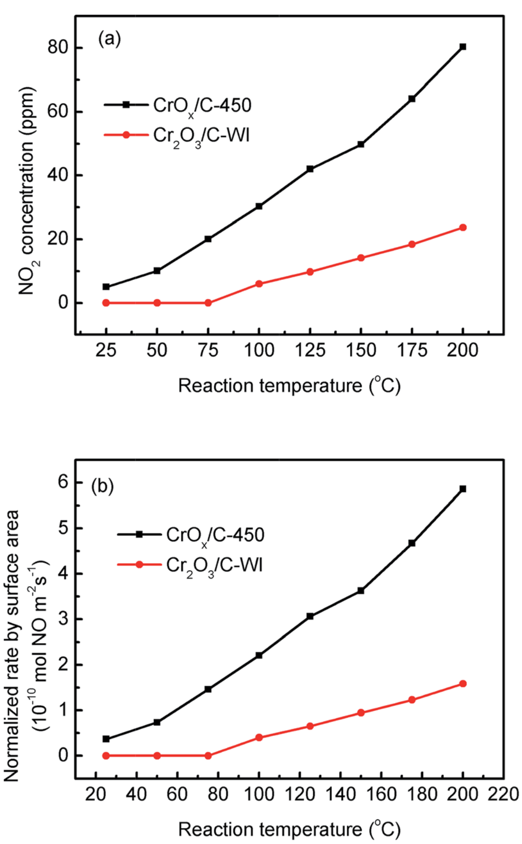

Fig. 7 (a) NO oxidation performances and (b) normalized NO oxidation rate by surface area on CrO_x/C-450 and C–Cr_2O_3 catalysts.

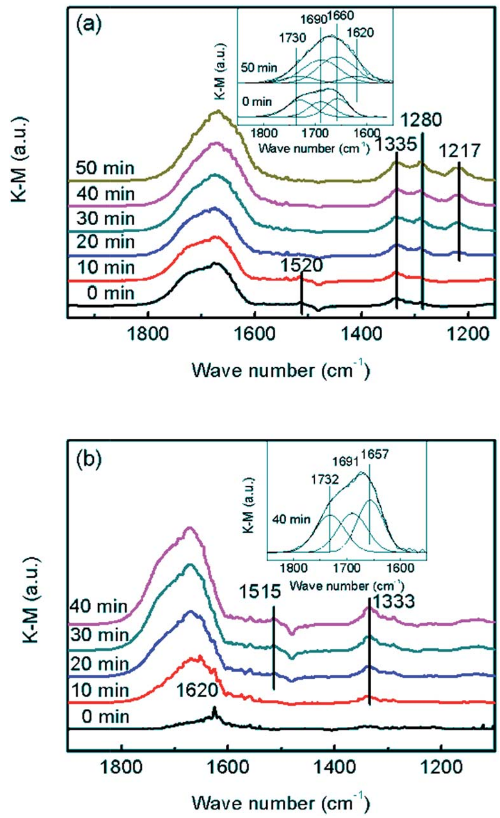

Fig. 8 *In situ* DRIFT spectra of CrO_x/C-450: (a) NH_3 reacted with pre-absorbed NO + O_2, (b) NO + O_2 reacted with pre-absorbed NH_3.

This indicated that NH_3 on Lewis sites was reacted and consumed. Therefore, the entire NH_3-SCR on CrO_x/C-450 followed a L–H mechanism, in which NO was oxidized by the unsaturated oxygen of CrO_x/C-450 catalyst and transformed to NO_2. The formed NO_2 further absorbed on the surface of CrO_x/C-450 as bidentate nitrates, and reacted with NH_3 on Lewis sites, forming N_2 and H_2O at last. Due to the formation of NO_2, the reaction proceeded as a "fast NH_3-SCR" pathway, causing the decrease in reaction activation energy, thus enhancing the low-temperature activity.

3.5. Reasons of excellent SO_2 tolerance of regeneration ability

Sulfation process is a transition from metal oxide to metal sulfate. Irrespective of which type of intermediate exists in the sulfation process, the metal–oxygen band must be broken. It is reasonable to deduce that a metal oxide with a strong metal–oxygen band is difficult to be sulfated. The Cr–O band energy of the eskolaite phase Cr_2O_3 was calculated (see the ESI†). As displayed in Table S5,† the band energy of the Cr–O band in the eskolaite phase Cr_2O_3 exceeds that of Mn–O band in MnO_2, indicating that the sulfation process of Cr_2O_3 proceeds with more difficulty as compare that of MnO_2. This is considered to be the result of the various NH_3-SCR performances of MnO_2 and CrO_x/C-450 catalyst in the presence of SO_2. Moreover, MnO_2 and CrO_x/C-450 catalysts deactivated by SO_2 were washed with deionized water and the metal-ion contents in the eluate were measured by ICP analysis. As presented in Table S6,† Mn^{2+} was detected in the eluate of the deactivated MnO_2 sample, while no Cr^{3+} was detected in the eluate of the deactivated CrO_x/C-450 sample. It is evident that the CrO_x/C-450 sample was protected from sulfation.

To further understand the SO_2 poisoning and regeneration processes, the XPS spectra of the fresh CrO_x/C-450 catalyst, SO_2-poisoned sample, and regenerated sample were studied. As displayed in Fig. 6a and Table 2, the Cr state and relative content of Cr^{6+} and Cr^{3+} of each sample were similar, which indicated that, as it is designed, CrO_x/C-450 catalyst was difficult to be sulfated for the high lattice energy of Cr_2O_3. Comparing the O 1s peak of the fresh CrO_x/C-450 sample and the regenerated sample (Fig. 6b), their peaks of lattice oxygen were similar and both shifted to the high binding energy side than that of bulk Cr_2O_3. Since activated lattice oxygen still remained on the surface, the regenerated catalyst exhibited high NH_3-SCR activity, similar to the fresh catalyst.

In XPS spectra of the SO_2 poisoned sample, the peaks of S 2p and N 1s were detected. The S 2p peak (Fig. S7a†) consists of two peaks at 168.5 eV (S $2p_{1/2}$) and 169.7 eV (S $2p_{3/2}$), which belonged to SO_4^{2-}. The N 1s spectra (Fig. S7b†) can be divided into two peaks at 399.5 eV and 400.5 eV, contributed to NH_3 and NH_4^+, respectively. According to the relative atom contents listed in Table S7,† atoms-ratio of SO_4^{2-} and NH_4^+ was nearly 1 : 1 on the surface of the SO_2-poisoned sample. This indicated that NH_4HSO_4 deposited on the surface of CrO_x/C-450 during the SO_2 poisoning process, which causes the deactivation of the catalyst. After heat treatment, the deposited NH_4HSO_4 could easily decompose and the CrO_x/C-450 catalyst with exposed activated lattice oxygen regains the superior activity.

4. Conclusions

In this study, we successfully designed and synthesized a novel chromium oxide nano-particles catalyst with excellent NH_3-SCR activity at 150 °C and remarkable SO_2 regenerative ability. The obtained CrO_x/C-450 catalyst was composed of CrO_x nano-particles covered by amorphous carbon. A carbon species, which was derived from the organic linkers of the MOFs precursor, protected the CrO_x nano-particles from aggregation. CrO_x/C catalysts primarily have Eskolaite phase Cr_2O_3 with average size of 3 nm and exhibit a large surface area. Due to the small size of CrO_x nano-particles in CrO_x/C catalysts, the lattice oxygen atoms of CrO_x/C were activated, so that NO could be oxidized to NO_2 on the catalyst surface. The formed NO_2 participated in reaction and made NH_3-SCR on CrO_x/C proceed through a "fast NH_3-SCR" pathway. The large surface area and activated lattice oxygen of CrO_x/C catalysts caused the enhanced NH_3-SCR activities. Due to the stable lattice of Cr_2O_3, CrO_x/C catalyst could hardly be sulfated in the SO_2 poisoning process. Therefore, the regenerated catalyst still retained prominent activity when NH_4HSO_4 deposited on the surface of the catalyst was removed during the regeneration process.

Conflicts of interest

There are no conflicts to declare.

Acknowledgements

The financial supports of National High-tech Research and Development (863) Program of China (2015AA03A401), National Natural Science Foundation of China (No. 21573105), Natural Science Foundation of Jiangsu Province (BK20161392), and Jiangsu Province Science and Technology Support Program (Industrial, BE2014130) are gratefully acknowledged.

References

1 C. Liu, J. W. Shi, C. Gao and C. M. Niu, *Appl. Catal., A*, 2016, **522**, 54–69.
2 T. H. Vuong, J. Radnik, E. Kondratenko, M. Schneider, U. Armbruster and A. Bruckner, *Appl. Catal., B*, 2016, **197**, 159–167.
3 T. H. Vuong, J. Radnik, M. Schneider, H. Atia, U. Armbruster and A. Bruckner, *Catal. Commun.*, 2016, **84**, 171–174.
4 C. J. Tang, H. L. Zhang and L. Dong, *Catal. Sci. Technol.*, 2016, **6**, 1248–1264.
5 S. Wu, X. Yao, L. Zhang, Y. Cao, W. Zou, L. Li, K. Ma, C. Tang, F. Gao and L. Dong, *Chem. Commun.*, 2015, **51**, 3470–3473.
6 K. Wijayanti, S. Andonova, A. Kumar, J. Li, K. Kamasamudram, N. W. Currier, A. Yezerets and L. Olsson, *Appl. Catal., B*, 2015, **166**, 568–579.
7 J. H. Lee, Y. J. Kim, T. Ryu, P. S. Kim, C. H. Kim and S. B. Hong, *Appl. Catal., B*, 2017, **200**, 428–438.
8 P. Chen, R. Moos and U. Simon, *J. Phys. Chem. C*, 2016, **120**, 25361–25370.
9 J. Liu, X. Li, Q. Zhao, J. Ke, H. Xiao, X. Lv, S. Liu, M. Tade and S. Wang, *Appl. Catal., B*, 2017, **200**, 297–308.
10 T. Boningari, P. R. Ettireddy, A. Somogyvari, Y. Liu, A. Vorontsov, C. A. McDonald and P. G. Smirniotis, *J. Catal.*, 2015, **325**, 145–155.
11 H. Hu, S. X. Cai, H. R. Li, L. Huang, L. Y. Shi and D. S. Zhang, *ACS Catal.*, 2015, **5**, 6069–6077.
12 Z. M. Liu, J. Z. Zhu, J. H. Li, L. L. Ma and S. I. Woo, *ACS Appl. Mater. Interfaces*, 2014, **6**, 14500–14508.
13 H. Chang, X. Chen, J. Li, L. Ma, C. Wang, C. Liu, J. W. Schwank and J. Hao, *Environ. Sci. Technol.*, 2013, **47**, 5294–5301.
14 J. Li, H. Chang, L. Ma, J. Hao and R. T. Yang, *Catal. Today*, 2011, **175**, 147–156.
15 C. Liu, L. Chen, J. Li, L. Ma, H. Arandiyan, Y. Du, J. Xu and J. Hao, *Environ. Sci. Technol.*, 2012, **46**, 6182–6189.
16 L. Zhang, L. L. Li, Y. Cao, X. J. Yao, C. Y. Ge, F. Gao, Y. Deng, C. J. Tang and L. Dong, *Appl. Catal., B*, 2015, **165**, 589–598.
17 D. W. Kwon, K. B. Nam and S. C. Hong, *Appl. Catal., B*, 2015, **166**, 37–44.
18 G. Qi and R. T. Yang, *Appl. Catal., B*, 2003, **44**, 217–225.
19 C. Liu, J.-W. Shi, C. Gao and C. Niu, *Appl. Catal., A*, 2016, **522**, 54–69.
20 M. Colombo, I. Nova, E. Tronconi, V. Schmeißer, B. Bandl-Konrad and L. Zimmermann, *Appl. Catal., B*, 2012, **111–112**, 106–118.
21 S. Roy, M. S. Hegde and G. Madras, *Appl. Energy*, 2009, **86**, 2283–2297.
22 B. Guan, R. Zhan, H. Lin and Z. Huang, *Appl. Therm. Eng.*, 2014, **66**, 395–414.
23 S. X. Cai, H. Hu, H. R. Li, L. Y. Shi and D. S. Zhang, *Nanoscale*, 2016, **8**, 3588–3598.
24 E. Rhodes and A. R. Ubbelohde, *Proc. R. Soc. A*, 1959, **251**, 156–171.
25 M. Kang, E. D. Park, J. M. Kim and J. E. Yie, *Catal. Today*, 2006, **111**, 236–241.
26 A. Zhou, D. Yu, L. Yang and Z. Sheng, *Appl. Surf. Sci.*, 2016, **378**, 167–173.
27 S. Xiong, X. Xiao, N. Huang, H. Dang, Y. Liao, S. Zou and S. Yang, *Environ. Sci. Technol.*, 2017, **51**, 531–539.
28 Q.-l. Chen, R.-t. Guo, Q.-s. Wang, W.-g. Pan, W.-h. Wang, N.-z. Yang, C.-z. Lu and S.-x. Wang, *Fuel*, 2016, **181**, 852–858.
29 H. E. Curry-Hyde, H. Musch and A. Baiker, *Appl. Catal.*, 1990, **65**, 211–223.
30 B. L. Duffy, H. E. Curry-Hyde, N. W. Cant and P. F. Nelson, *J. Catal.*, 1994, **149**, 11–22.
31 G. Busca, L. Lietti, G. Ramis and F. Berti, *Appl. Catal., B*, 1998, **18**, 1–36.
32 G. Marban, R. Antuna and A. B. Fuertes, *Appl. Catal., B*, 2003, **41**, 323–338.
33 E. Curry-Hyde and A. Baiker, *Ind. Eng. Chem. Res.*, 1990, **29**, 1985–1989.
34 S. Alayoglu, A. U. Nilekar, M. Mavrikakis and B. Eichhorn, *Nat. Mater.*, 2008, **7**, 333–338.
35 K. Yamamoto, T. Imaoka, W. J. Chun, O. Enoki, H. Katoh, M. Takenaga and A. Sonoi, *Nat. Chem.*, 2009, **1**, 397–402.
36 C. T. Campbell and Z. Mao, *ACS Catal.*, 2017, **7**, 8460–8466.
37 K. Shen, X. Chen, J. Chen and Y. Li, *ACS Catal.*, 2016, **6**, 5887–5903.
38 P. Yin, T. Yao, Y. Wu, L. Zheng, Y. Lin, W. Liu, H. Ju, J. Zhu, X. Hong, Z. Deng, G. Zhou, S. Wei and Y. Li, *Angew. Chem., Int. Ed. Engl.*, 2016, **55**, 10800–10805.
39 P. Mahata, D. Sarma, C. Madhu, A. Sundaresen and S. Natarajan, *Dalton Trans.*, 2011, **40**, 1952–1960.
40 P. Yin, T. Yao, Y. Wu, L. Zheng, Y. Lin, W. Liu, H. Ju, J. Zhu, X. Hong, Z. Deng, G. Zhou, S. Wei and Y. Li, *Angew. Chem., Int. Ed.*, 2016, **55**, 10800–10805.
41 B. You, N. Jiang, M. Sheng, W. S. Drisdell, J. Yano and Y. Sun, *ACS Catal.*, 2015, **5**, 7068–7076.
42 J. Yu, F. Guo, Y. Wang, J. Zhu, Y. Liu, F. Su, S. Gao and G. Xu, *Appl. Catal., B*, 2010, **95**, 160–168.
43 S. H. Jhung, J. H. Lee, J. W. Yoon, C. Serre, G. Ferey and J. S. Chang, *Adv. Mater.*, 2007, **19**, 121–124.
44 A. Henschel, K. Gedrich, R. Kraehnert and S. Kaskel, *Chem. Commun.*, 2008, 4192–4194.
45 O. Kouvo and Y. Vuorelainen, *Am. Mineral.*, 1958, **43**, 1098–1106.
46 F. Ayari, M. Mhamdi, D. P. Debecker, E. M. Gaigneaux, J. Alvarez-Rodriguez, A. Guerrero-Ruiz, G. Delahay and A. Ghorbel, *J. Mol. Catal. A: Chem.*, 2011, **339**, 8–16.

47 M. A. Henderson and M. H. Engelhard, *J. Phys. Chem. B*, 2014, **118**, 29058–29067.

48 B. Wichterlova, L. Krajcikova, Z. Tvaruzkova and S. Beran, *J. Chem. Soc., Faraday Trans. 1*, 1984, **80**, 2639–2645.

49 D. Shuttleworth, *J. Phys. Chem.*, 1980, **84**, 1629–1634.

50 T. Dickinson, A. F. Povey and P. M. A. Sherwood, *J. Chem. Soc., Faraday Trans.*, 1976, **72**, 686–705.

51 K. I. Hadjiivanov, *Catal. Rev.*, 2000, **42**, 71–144.

52 X. Li, X. Li, J. Li and J. Hao, *J. Hazard. Mater.*, 2016, **318**, 615–622.

53 Z. Liu, S. Zhang, J. Li and L. Ma, *Appl. Catal., B*, 2014, **144**, 90–95.

54 Y. An, Y. Liu, P. An, J. Dong, B. Xu, Y. Dai, X. Qin, X. Zhang, M.-H. Whangbo and B. Huang, *Angew. Chem., Int. Ed. Engl.*, 2017, **56**, 3036–3040.